Available online at www.sciencedirect.com
ScienceDirect
Acta Materialia 55 (2007) 273–284
Acta MATERIALIA
www.actamat-journals.com

Heat treatment-modulated coupling effect of multi-scale second-phase particles on the ductile fracture of aged aluminum alloys

G. Liu [a], G.J. Zhang [a], R.H. Wang [a], W. Hu [a], J. Sun [a,*], K.H. Chen [b]

[a] *State Key Laboratory for Mechanical Behavior of Materials, School of Material Science and Engineering, Xi'an Jiaotong University, Xiang Ning Xi Lu 28#, Xi'an, ShanXi 710049, China*

[b] *State Key Laboratory for Powder Metallurgy, The University of Southern Central China, Changsha 410083, China*

Received 9 September 2005; received in revised form 14 June 2006; accepted 8 August 2006
Available online 24 October 2006

Abstract

Experiments and multi-scale modeling were carried out in order to study the heat treatment-modulated coupling effect of multi-scale second-phase particles on the ductile fracture of two typical kinds of heat-treatable aluminum alloys, i.e. an Al–Cu–Mg alloy and an Al–Mg–Si alloy. It was revealed experimentally and theoretically that an appropriate combination of the multi-scale second-phase particles, which could be achieved by appropriate cooperation of the heat treatment steps, i.e. the solution, quenching and aging treatments, is necessary and sufficient for obtaining an excellent fracture toughness for the heat-treatable aluminum alloys. The experimental phenomenon, that the alloys containing more detrimental constituents but aged at a somewhat higher temperature exhibit ductility and fracture toughness superior to those of the alloys containing less detrimental constituents but aged at lower temperatures, could be reasonably explained by the cooperative effect of the heat treatment steps. Contours of the fracture toughness with respect to the technological parameters of the heat treatment, e.g. the aging temperature and quench factor, were developed to show the cooperative effect of the heat treatment steps on the fracture toughness of the aged aluminum alloys quantitatively. The good agreement between the calculations and the experimental results indicated that the present modeling is applicable for describing the heat treatment-modulated coupling effect of the multi-scale second-phase particles in aged aluminum alloys.

Keywords: Aluminum alloys; Toughness; Precipitation; Modeling; Quenching

1. Introduction

Heat-treatable aluminum alloys, which are the backbone of the aircraft industry, exhibit mechanical properties that are closely dependent on second-phase particles and are remarkably sensitive to heat treatment, i.e. the three-step process of solution, quenching and aging treatments. Because the second-phase particles in aged aluminum alloys are associated with the heat treatment steps directly, the good understanding of the influence of the second-phase particles on the ductile fracture of aged aluminum alloys could be used for promoting the controlling of the ductility and fracture toughness of aged aluminum alloys by adjusting the heat treatment steps artificially, which is an everlasting pursuit in heat-treatable aluminum alloys.

Heat-treatable aluminum alloys normally contain three classes of second-phase particles that are of multi-scale sizes and have different shapes [1–3]: coarse ellipse-shaped constituents of ~1–10 μm in diameter, intermediate sphere-shaped dispersoids of ~0.05–0.5 μm in diameter and fine disc-/plate- or needle-/rod-shaped strengthening precipitates several tens of nanometers thinner in size. The brittle constituents are ready to crack at lower strain and so nucleate large voids. Under further deformation, these voids grow in size up to coalescence where the fracture is triggered. The coalescence of voids is often rate limited by the rupture of the intermediate ligament and

* Corresponding author. Tel.: +86 29 82667143; fax: +86 29 82663453.
E-mail address: junsun@mail.xjtu.edu.cn (J. Sun).

1359-6454/$30.00
doi:10.1016/j.actamat.2006.08.026

experiments have suggested that the void sheets formed by dispersoids link the larger failure sites around constituents [4,5]. This process depends on the size and volume fraction of the dispersoids, the cohesive strength of the matrix/dispersoids and the coherency and shearability of the precipitates [1–4]. From a metallographic point of view, Fig. 1 typically illustrates the close dependence of ductile fractures on the three classes of second-phase particles in a multi-length manner, where the larger voids nucleated by the cracking of micrometer-sized constituents, the void sheet caused by decohesion of the sub-micrometer-sized dispersoids and the ligament strengthened by the nanometer-sized precipitates are presented on different length scales, respectively.

Extensive work [1–3,6–10] has been carried out in order to study the influence of the three classes of second-phase particles on the ductile fractures of aged aluminum alloys, where most attention was paid to the separate effects of the three classes of second-phase particles on the ductile fractures of aged aluminum alloys. However, it is not enough to consider only the separate effects because some significant coupling interactions exist among these multi-scale second-phase particles. In order to improve the physical insight into the ductile fractures of heat-treatable aluminum alloys, the coupling effects or combined effects of the multi-scale second-phase particles need to be well understood so as to reveal the nonlinear interactions among the micro-structural features, from micrometer-scale length to nanometer-scale length. Recently, a multi-scale model [11,12] has been developed by the authors for describing both the separate and coupling effects of the three classes of second-phase particles on the ductile fractures of aged aluminum alloys by using a unified expression, where the parameters (e.g. volume fraction, size and aspect ratio) of all the particles were taken into account. In this model, the macro-strain to fracture of samples was firstly related to the micro-scale broken constituents on the basis of the fracture mechanics. Subsequently, the critical local strain for rupture of a ligament between two neighboring broken constituents was developed as a function of the parameters of both sub-micron-scale dispersoids and nano-scale precipitates by using the treatment of geometrically necessary dislocations [11]. This makes the multi-scale model cover from the micrometer scale to the nanometer scale and yield a unified expression that is a nonlinear function of the parameters of all the three classes of second-phase particles. In application to experimental data, the separate influences of the three classes of second-phase particles on ductile fractures have been well described by this model [11]. In addition, some coupling effects of the trade-off in the volume fraction between the second-phase particles, which could be obtained by adjusting the heat treatment steps, could also be analyzed using this model. For example, analytical results have revealed that the dependence of the ductility of commercial heat-treatable aluminum alloys was non-monotonic on the trade-off in volume fraction between the constituents and the precipitates that was caused by adjusting the solution treatment, which is in good agreement with the experimental results [12]. This means that reducing the volume fraction of the constituents is not enough to enhance the ductility when considering the coupling effect of the constituents and precipitates. What is further indicated from the analytical results is that, in order to obtain excellent

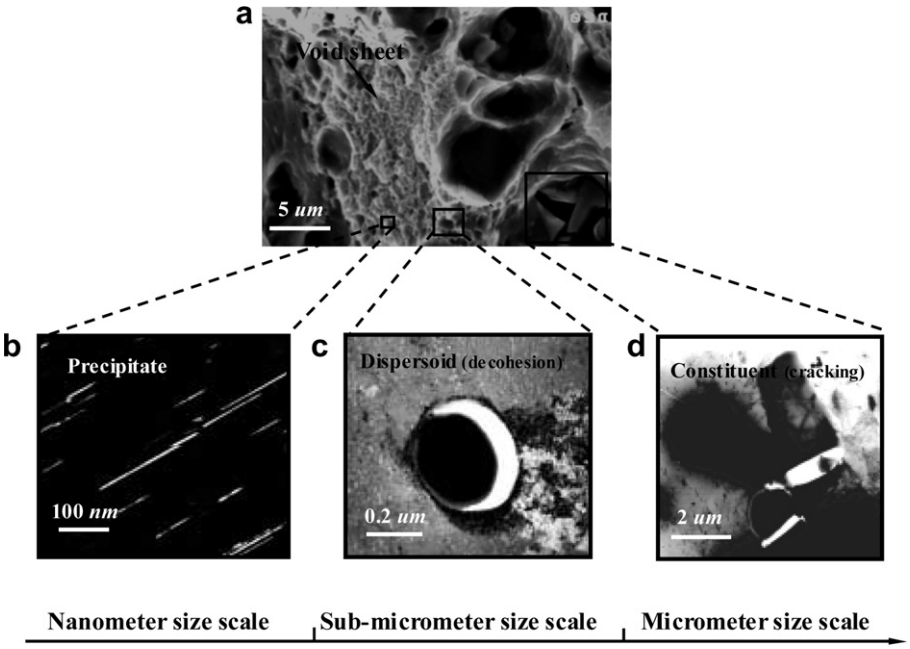

Fig. 1. SEM and TEM images illustrating the close dependence of the ductile fracture of the Al–Cu–Mg alloy on the three classes of second-phase particles in a multi-length manner and from a metallographic point of view, i.e. (a) a typical fracture surface SEM micrograph showing (b) the ligament strengthened by the nanometer-sized precipitates (dark field image), (c) the void sheet caused by decohesion of the sub-micrometer-sized dispersoids and (d) larger voids nucleated by the cracking of the micrometer-sized constituents.

mechanical properties for commercial heat-treatable aluminum alloys, an appropriate coupling effect of the multi-scale second-phase particles could be artificially assembled by tailoring the combination of these second-phase particles in order to produce optimum coupling interactions.

The artificial tailoring of the second-phase particles could be achieved by adjusting the heat treatment steps. It is well known that, besides the strengthening precipitates that are directly controlled by the three heat treatment steps, the constituents and the dispersoids should also be significantly influenced by the solution and quench treatments. The parameters of the three classes of second-phase particles, particularly of the precipitates, could be modulated artificially by employing different heat treatment steps, respectively. It is then possible to produce an appropriate coupling effect of the multi-scale second-phase particles and obtain some desired mechanical properties for aged aluminum alloys by adjusting the heat treatment steps. As a result, the capability for controlling the ductility and fracture toughness of aged aluminum alloys artificially could be significantly promoted by understanding the cooperative effect of the heat treatment steps or the coupling effect of the multi-scale second-phase particles on the ductile fractures of aged aluminum alloys.

Recently, increasing attention has been paid to describing the quantitative influence of the heat treatment steps on the evolution of second-phase particles, including the dispersoids [13–15] and the precipitates [16–21], in age-hardening aluminum alloys. Some mathematical relations have been developed for relating the hardness (or yield strength) of aged aluminum alloys to the evolution of the precipitates or to the heat treatment in industrial processing by using process models [16–24]. This provides some theoretical bases and ongoing direction for modeling the dependence of the ductile fractures of aged aluminum alloys on the heat treatment-modulated dynamic evolution of the second-phase particles, which could be related to the heat treatment directly.

In this study, both experiments and analytical modeling were carried out in order to study the dependence of ductile fractures on the heat treatment-modulated coupling effect of the multi-scale second-phase particles in aged aluminum alloys. The experiments were focused on the influence of different heat treatment steps, including different solution treatments, quenching treatments and aging treatments, on the ductility and fracture toughness of two typical heat-treatable aluminum alloys, i.e. an Al–Cu–Mg alloy, which contains disc- or plate-shaped strengthening precipitates and an Al–Mg–Si alloy, which contains rod- or needle-shaped strengthening precipitates. Three types of solution plus quenching treatments followed by a series of aging treatments were applied to the two aluminum alloys in order to achieve different combinations of the multi-scale second-phase particles. The changes in the volume fractions and aspect ratios of the second-phase particles as well as the changes in the quasi-stationary mechanical properties were experimentally measured for comparison. A multi-scale model [11] was improved by combining it with an aging-strengthening model [25], which was based on the strengthening expressions for aluminum alloys containing plate- or rod-shaped precipitates [26], in order to analyze the heat treatment-modulated coupling effect of the multi-scale second-phase particles. In addition, the relationship between the fracture toughness and yield strength of the two types of aged aluminum alloys was obtained both experimentally and theoretically. The good agreement between the calculations and the experimental results showed that the coupling effect of the multi-scale second-phase particles, which could be artificially modulated by adjusting the heat treatment, could bring about more choices of mechanical properties for aged aluminum alloys in order to meet the multiplex needs in industrial technologies.

2. Experimental procedures

The aluminum alloys used in the present investigation were hot-rolled Al–Cu–Mg plate of 16 mm thickness and extruded Al–Cu–Mg and Al–Mg–Si rods each of 18 mm diameter, which were supplied by the research laboratory of Xi'an Air Craft Industry Ltd. The Al–Cu–Mg plate and the Al–Cu–Mg rod were from the same ingot. The composition in weight percentages were 4.62% Cu, 0.65% Mg, 0.22% Mn, 0.08% Si, 0.1% Fe, 0.1% Zn and balance Al for the Al–Cu–Mg alloy and 1.12% Mg, 0.57% Si, 0.25% Cu, 0.22% Cr and balance Al for the Al–Mg–Si alloy.

Three types of solution plus quenching treatments, i.e. an enhanced solution plus fast quenching treatment (EF), a traditional solution plus fast quenching treatment (TF) and a traditional solution plus slow quenching treatment (TS), were applied to the two aluminum alloys in order to achieve a change in the volume fraction of the three classes of the second-phase particles. The enhanced solution or stepped solution was employed for dissolving more soluble constituents and dispersoids as possible while the application of slow quench would induce more constituents and dispersoids. A series of aging treatments were subsequently applied in order to produce different combinations of the precipitates with the other two classes of second-phase particles. The detailed heat treatments were as follows. The traditional solution treatments of the Al–Cu–Mg and Al–Mg–Si alloys were held at 766 K for 2 h and at 703 K for 30 min, respectively. The fast quenching treatment referred to quenching into cold water while the slow quenching treatment meant cooling with a controlled rate of 5 K/s. The enhanced solution treatment for the Al–Cu–Mg alloy was firstly held at 766 K for 2 h and then followed by being held at an increasing treatment temperature of up to 776 K at a rate of 4 K/h and that for the Al–Mg–Si alloy was firstly held at 703 K for 30 min and then followed by being held at an increasing treatment temperature of up to 708 K at a rate of 7 K/h. The Al–Cu–Mg and Al–Mg–Si alloys were artificially aged at 483 K, 513 K and 543 K and at

433 K, 463 K and 493 K, respectively, for various times from 15 min to 10 days in order to obtain different aging conditions. The maximum error of all the temperature measurements in the present experiments was ±1 K.

The yield strength, strain to fracture and strain-hardening exponent of the different heat-treated alloys were measured by using a smooth dog bone-shaped tensile specimen that had a gauge size of 6 mm in diameter and 40 mm in length. All of the specimens had an axis along the longitudinal direction. The tensile test was performed at a constant strain rate of 5×10^{-4}/s with the load direction parallel to the specimen axis. The yield stress was determined as the 0.2% offset and the strain to fracture was determined as $\varepsilon_f = \ln(A_0/A_f)$, where A_0 is the initial area and A_f is the area at fracture of the specimens.

The fracture toughness of the Al–Cu–Mg alloys was characterized with compact tension specimens and the R curve method. Only the L–T-oriented specimens having a fracture plane normalized to the longitudinal direction of the plate and an expected direction of a through thickness crack propagation coincident with the width direction of the plate were measured with applied loading along with the longitudinal direction. All the specimens were the same size at 62.5 mm in width and 6.25 mm in thickness. Prior to the fracture toughness experiment, the specimens were fatigue pre-cracked at a constant stress ratio ($R = K_{min}/K_{max}$) of 0.1 and under a decreasing stress intensity condition. Strictly conforming to ASTM E561, the R-curve characterization of fracture toughness was performed on a servohydraulic Instron-type testing machine by using the potential-drop method for measuring the crack length. The crack growth resistance curve was recorded and the plane strain fracture toughness was determined at fracture initiation [27]. All the geometry requirements for the plane strain constraint were met and the obtained plane strain fracture toughness from the R-curve was experimentally found to be approximately equal to that determined according to ASTM E399.

Based on quantitative microscopy [28], the size and volume fraction of the constituents and dispersoids were quantitatively measured by using scanning electron microscopy (SEM) and transmission electron microscopy (TEM),

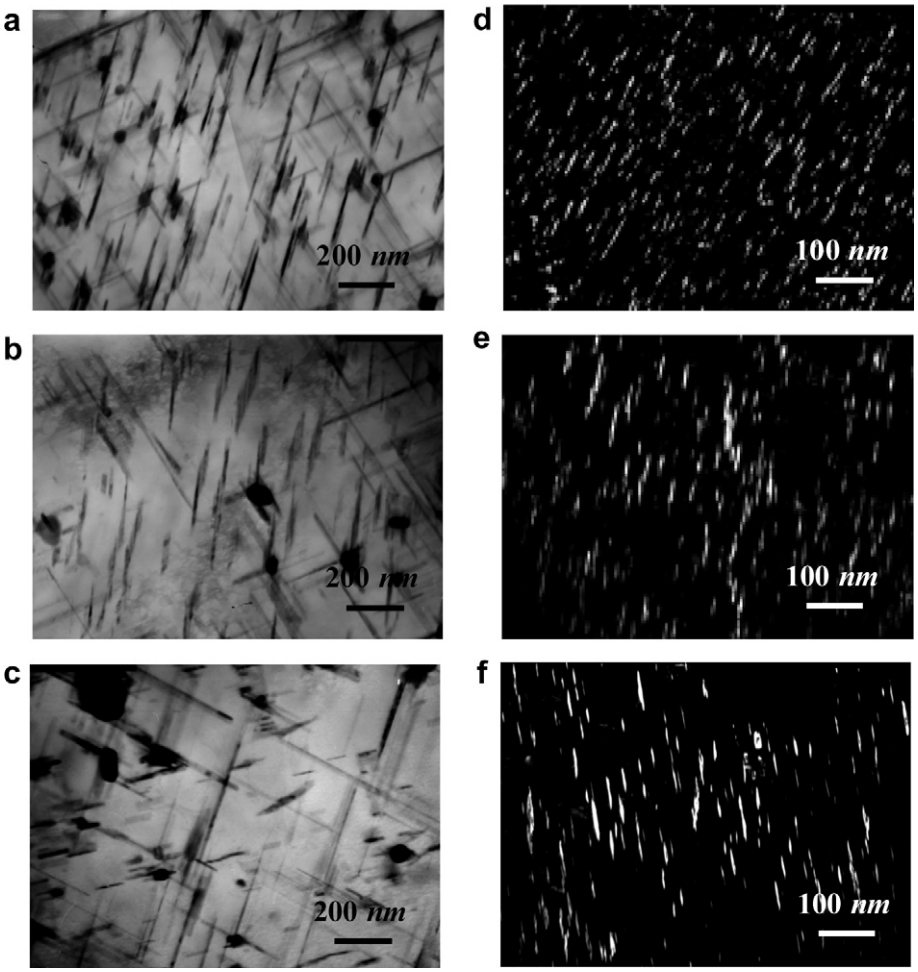

Fig. 2. Typical images of the plate-/disc-shaped precipitates (bright field image) in the TF-treated Al–Cu–Mg alloys that were peak aged at (a) 483 K, (b) 513 K and (c) 543 K and of the rod-/needle-shaped precipitates (dark field image) in the TF-treated Al–Mg–Si alloys that were peak aged at (d) 433 K, (e) 463 K and (f) 493 K.

respectively [11,12]. Thin foils for micro-structural characterization by TEM were prepared by mechanical thinning with SiC paper to 100 μm, followed by electro-polishing with an applied potential of 15 V in a 3:1 methanol:nitric solution cooled to –25 °C. Prepared samples were rinsed twice in methanol, dried and examined immediately in a JEOL Ltd JEM-200CX TEM at 100 kV. By using the TEM examination, the size and volume fractions of the precipitates were determined from at least 600 random precipitates seen edge on. As the thicker dimensions of the precipitates, i.e. the radius (r) of the plate-shaped precipitates in the Al–Cu–Mg alloys or the half length (l) of the rod-/needle-shaped precipitates in the Al–Mg–Si alloys, were of the same order and sometimes greater than the thickness of the thin foil, a correction was employed for differentiating the real dimension from the observed one [29] and the volume fraction (f_p) of the oriented precipitates in a thin-foil projection (corrected for truncation and overlap) was determined by [30]

$$f_p = \left(\frac{-2\pi r}{\pi r + 4h}\right) \ln(1 - A_A), \quad (1)$$

where r is the radius of the plate-shaped precipitates (replaced by l for the rod-shaped precipitates), h is the foil thickness and A_A is the projected area fraction of the precipitates, as determined by the point count method. The foil thickness was easily obtained by utilizing a grain boundary fringes technique [31].

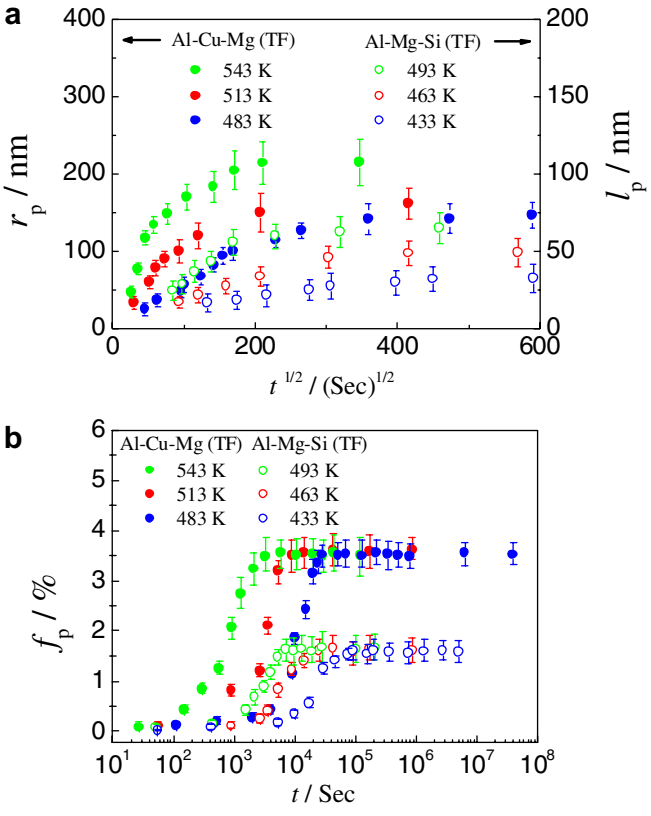

Fig. 3. (a) Dependence of the radius (r_p) of the disc-/plate-shaped precipitates in the TF-treated Al–Cu–Mg alloys (left y-axis) and the half-length (l_p) of the rod-/needle-shaped precipitates in the TF-treated Al–Mg–Si alloys (right y-axis). (b) Dependence of the volume fraction of the precipitates in the two kinds of alloys on the aging temperature (T) as a function of the aging time (t).

3. Experimental results

3.1. Microstructures

Experimental results have revealed that there are some noticeable changes in second-phase particles after the three kinds of solution/quenching treatments [12]. Speaking in detail, the EF treatment should reduce the volume fraction of the constituents (f_c) but increase the volume fraction of precipitates (f_p), while the TS treatment should induce a larger value for f_c but a small value for f_p, compared with the TF treatment. This means that the application of these three kinds of treatments could produce different combinations of constituents and precipitates in the volume fraction or produce a trade-off between f_c and f_p. In the present work, various aging treatments were applied to put out different growth evolutions of the precipitates and induce different combinations of the multi-scale second-phase particles, particularly in size.

Figs. 2a–c and d–f show some typical images of the plate-/disc-shaped precipitates (bright field image) in the

Table 1
Parameters of precipitates for the two alloys[a]

Alloys/treatment	r_p (l_p) (nm)	k_p	f_p (vol.%)
Al–Cu–Mg			
483 K			
EF	91(6)[b]	16.3(2.1)	6.34(0.27)
TF	102(8)	20.8(2.5)	3.61(0.19)
TS	109(11)	24.4(4.2)	3.09(0.11)
513 K			
EF	105(8)	19.2(2.7)	6.21(0.44)
TF	118(11)	24.2(3.2)	3.64(0.26)
TS	130(14)	28.5(4.1)	3.02(0.18)
543 K			
EF	111(15)	26.5(3.6)	6.25(0.52)
TF	127(17)	29.1(4.6)	3.59(0.31)
TS	142(21)	32.8(6.2)	3.04(0.22)
Al–Mg–Si			
433 K			
EF	24(2.5)	26.1(2.3)	2.68(0.18)
TF	27(4.2)	28.6(2.2)	1.80(0.15)
TS	32(4.8)	31.3(3.5)	1.44(0.25)
463 K			
EF	31(2.2)	30.6(1.8)	2.71(0.14)
TF	35(5.1)	33.1(4.7)	1.78(0.21)
TS	37(9.2)	37.3(6.2)	1.42(0.29)
493 K			
EF	36(4.7)	33.4(3.5)	2.66(0.17)
TF	8(7.4)	337.2(6.2)	1.77(0.20)
TS	42(9.5)	39.7(8.1)	1.34(0.25)

[a] All at peak-aging conditions.
[b] The values in parentheses are standard deviations.

FT-treated Al–Cu–Mg alloys that were peak aged at 483 K, 513 K and 543 K and of the rod-/needle-shaped precipitates (dark field image for clarity) in the FT-treated Al–Mg–Si alloys that were peak aged at 433 K, 463 K and 493 K, respectively. Quantitative examinations revealed that, when aged at a higher temperature, the precipitates in both the Al–Cu–Mg alloys and Al–Mg–Si alloys should exhibit a larger growth rate and so have a larger size, as shown in Fig. 3a. Moreover, a faster increasing rate of f_p and somewhat earlier achievement of the maximum value of f_p will result when aged at a higher aging temperature (see Fig. 3b). These trends were found not only in the TF-treated samples but also in the other two kinds of heat-treated samples, i.e. the EF-treated and TS-treated samples. A larger driving force for precipitation at higher aging temperatures should be responsible for the larger size and the faster precipitation rate of the strengthening second-phase particles. In contrast, the growth rate and size of the precipitates are less sensitive to solute content compared to the aging temperature [32]. Some further comparisons of the parameters of the precipitates for the two kinds of aluminum alloys that underwent different solution/quenching treatments and were aged at different temperature are listed in Table 1, where only the parameters of peak-aged samples are presented for simplicity.

The different evolutions of the precipitates with various aging treatments could put out different combinations of the multi-scale second-phase particles in both their size and volume fractions, which may result in some distinct coupling effects of the three classes of second-phase particles.

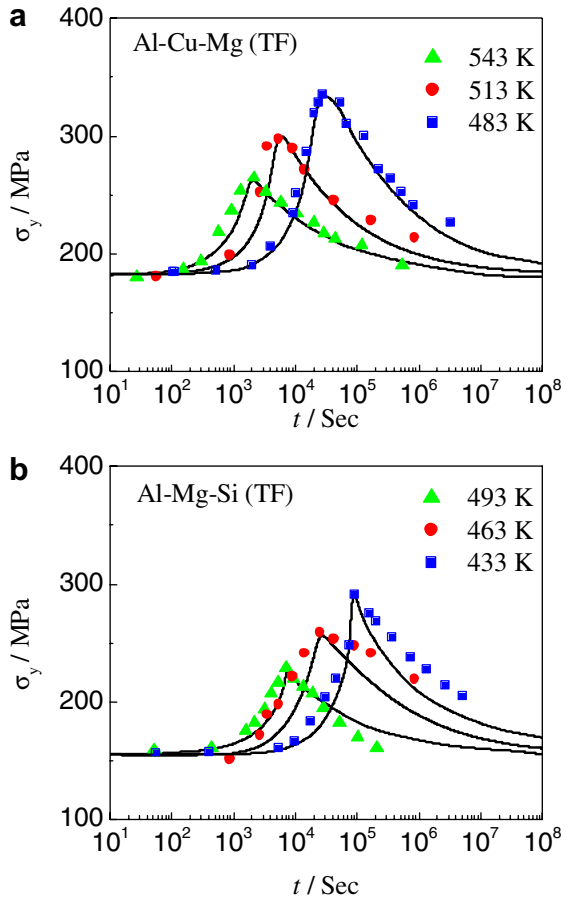

Fig. 4. Dependence of the yield strength (σ_y) on the aging temperature (T) as a function of the aging time (t) for (a) the TF-treated Al–Cu–Mg alloy and (b) the TF-treated Al–Mg–Si alloy. The triangles (green), circles (red) and squares (blue) in (a) and (b) are the experimental results of specimens aged at 543 K, 513 K and 483 K (Al–Cu–Mg alloy) and 493 K, 463 K and 433 K (Al–Mg–Si alloy), respectively and the curves are the calculated results. (For interpretation of the references to color in this figure legend, the reader is referred to the web version of this article.)

3.2. Mechanical properties

The dependence of the yield strength on the aging temperature as a function of the aging time was experimentally measured for the two aluminum alloys from the smooth tensile specimens, as typically shown in Figs. 4a and b for the TF-treated Al–Cu–Mg alloy and Al–Mg–Si alloy (dots). As mentioned earlier, when aged at a higher aging temperature, the strengthening second-phase particles should precipitate faster and grow larger, which makes the peak-aged condition occur at a somewhat shorter aging time and exhibit some lower peak yield strength. This is applicable for all of the three types of alloy with different

Table 2
Mechanical properties of the two alloys with different treatments[a]

Alloys/treatment	σ_y (MPa)	ε_f	K_{IC} (MPa m$^{1/2}$)
Al–Cu–Mg			
483 K			
EF	407	0.355	33.26
TF	334	0.287	26.78
TS	286	0.331	25.06
513 K			
EF	353	0.289	28.43
TF	298	0.237	22.68
TS	258	0.249	19.91
543 K			
EF	328	0.197	21.60
TF	264	0.180	19.53
TS	227	0.187	17.71
Al–Mg–Si			
433 K			
EF	336	0.402	–
TF	291	0.330	–
TS	248	0.341	–
463 K			
EF	292	0.343	–
TF	259	0.275	–
TS	225	0.288	–
493 K			
EF	267	0.257	–
TF	228	0.219	–
TS	205	0.227	–

[a] All at peak-aging conditions.

solution plus quenching treatments. The curves in Fig. 4 were calculated by using a recent strengthening model [25] together with some calibrated parameters from the experiments, which are in good agreement with the measured values.

The strain to fracture (ε_f) and the fracture toughness (K_{IC}) of the aluminum alloys were measured from the smooth tensile specimens and compact tension specimens, respectively. The variations of ε_f and K_{IC} with the aging time (t) at different aging temperature (T) were experimentally obtained by using a series of continuous measurements. In further treatments, the values of ε_f and K_{IC} at the peak-aged condition were summarized, as listed in Table 2. Fig. 5 shows the evolution of ε_f with the aging temperature as a function of the aging time for the TF-treated Al–Cu–Mg and Al–Mg–Si alloys, respectively. It is indicated from Fig. 5 that, although the samples aged at a lower temperature should have a greater ε_f in the under-aged conditions, they have smaller ε_f values in the peak-aged and over-aged conditions compared with the samples aged at higher temperatures. A similar trend was also found in the evolution of K_{IC}, as typically shown in Fig. 6a. Due to the significant influence of the aging temperature, the alloy containing a greater volume fraction of detrimental constituents but aged at somewhat higher temperature may have a fracture toughness greater than that of the alloy containing a smaller volume fraction of constituents but aged at lower temperatures. This conclusion can be explicitly shown in Fig. 6b, where the TS-treated Al–Cu–Mg alloy that was peak aged at 543 K has a greater fracture toughness than the EF-treated one that was peak aged at 483 K. Moreover, the former alloy exhibits a fracture toughness greater than the latter alloy at all the over-aged conditions. A further indication from these results is that only reducing the volume fraction of the constituents or detrimental inclusions

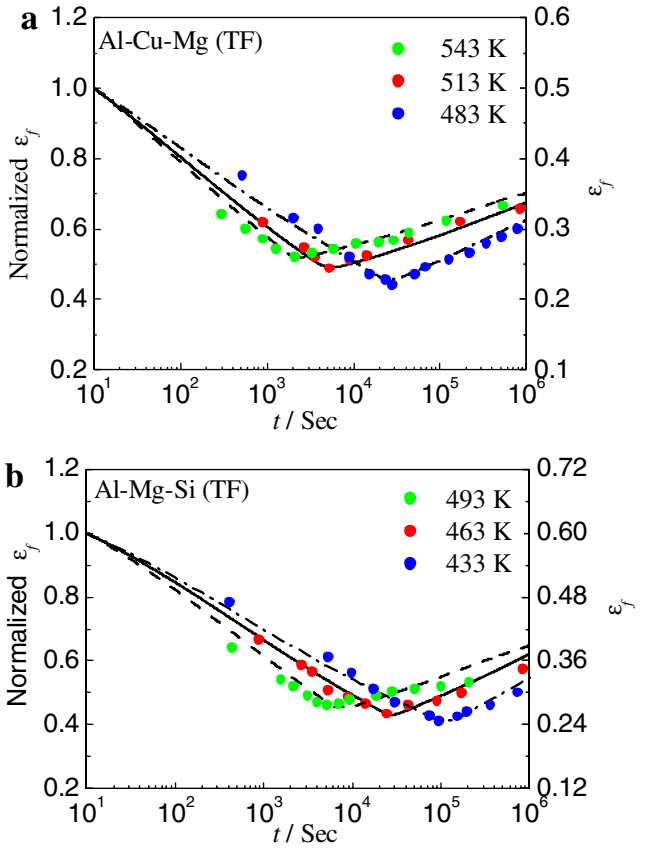

Fig. 5. Dependence of the strain to fracture (ε_f) on the aging temperature (T) as a function of the aging time (t) for (a) the TF-treated Al–Cu–Mg alloy and (b) the TF-treated Al–Mg–Si alloy. The green, red and blue solid dots in (a) and (b) are the experimental results of specimens aged at 543 K, 513 K and 483 K (Al–Cu–Mg) and 493 K, 463 K and 433 K (Al–Mg–Si alloy), respectively. The curves are the calculated results and the reference strain to fracture ε_f^R is that of the as-solution/quenching-treated alloys. (For interpretation of the references to color in this figure legend, the reader is referred to the web version of this article.)

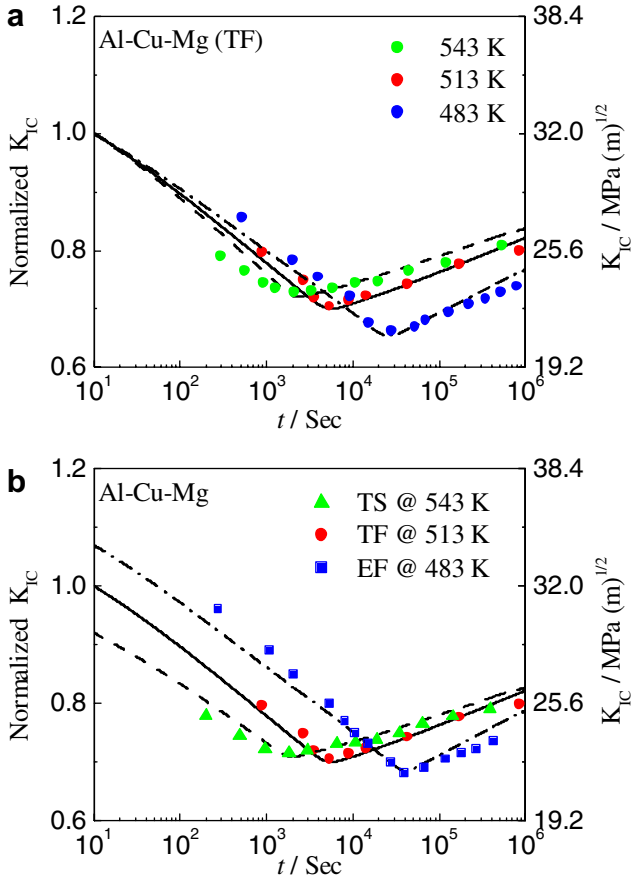

Fig. 6. (a) Dependence of the fracture toughness (K_{IC}) on the aging temperature (T) as a function of the aging time (t) for the TF-treated Al–Cu–Mg alloy. The green, red and blue solid dots are the experimental results of the TF-treated Al–Cu–Mg alloy aged at 543 K, 513 K and 483 K, respectively. (b) Dependence of the fracture toughness (K_{IC}) on the coupling effect of the aging temperature (T) and the solution/quenching treatment(s) as a function of the aging time (t) for the Al–Cu–Mg alloy. The triangles (green), circles (red) and squares (blue) are the experimental results of the TS-treated sample aged at 543 K, the TF-treated sample aged at 513 K and the EF-treated sample aged at 483 K, respectively. The curves are the calculated results. The reference strain to fracture ε_f^R is that of the TF-treated alloys at the as-solution/quenching-treated condition. (For interpretation of the references to color in this figure legend, the reader is referred to the web version of this article.)

by improving the solution and quenching treatments is not enough to achieve an excellent fracture resistance: an appropriate tailoring of the multi-scale second-phase particles or cooperation of all the solution, quench and aging treatments is necessary for optimizing the fracture resistance of commercial heat-treatable aluminum alloys.

At this point it is necessary to note that, in Figs. 5 and 6, all the curves were calculated by using the authors' multi-scale fracture model and strengthening model, which will be discussed later.

4. Discussion

4.1. Aging-modulated coupling effect of multi-scale second-phase particles

For the present alloys, the experiments revealed that the fracture mode of all the samples was predominantly in an intra-granular manner. Therefore, it is reasonable to conclude that the dependence of the ε_f and K_{IC} values of aluminum alloys on the aging treatment mainly results from the aging-modulated coupling effect of the multi-scale second-phase particles or the aging-tailored combination of the second-phase particles in different sizes. Quantitatively, the dependence of ε_f and K_{IC} on the three classes of second-phase particles intrinsically contained in commercial heat-treatable aluminum alloys could be described as [11]

$$\varepsilon_f = \frac{b\rho_g^c}{2\tilde{\varepsilon}_e(\theta)}\left[\frac{I}{0.405\pi h}\right]^{\frac{1}{n+1}}\left[\frac{\lambda_c}{2r_c}-1\right]^{\frac{1}{n+1}}(\lambda_d+\lambda_p)^{-1} \times\sqrt{[(1.7r_d\lambda_p)^2+(0.25\lambda_d\lambda_p)^2]}, \quad (2)$$

and

$$K_{IC} = \Gamma\sqrt{Bn^2\sigma_y\left[\frac{\lambda_c}{2r_c}-1\right]^{\frac{1}{n+1}}[(1.7r_d\lambda_p)^2+(0.25\lambda_p\lambda_d)^2]^{1/2}(\lambda_d+\lambda_p)^{-1}}, \quad (3)$$

where all the parameters have been clearly defined. Because the absolute values of some of the parameters, such as ρ_g^c and $\tilde{\varepsilon}_e(\theta)$, are difficult to determine while all of these parameters could be approximately regarded as constants, the strain to fracture and fracture toughness calculated here are normalized, i.e. divided by a reference strain to fracture (ε_f^R) and fracture toughness (K_{IC}^R), respectively, to eliminate these unknown parameters, as was done in our previous works [11,12]. The ε_f^R and K_{IC}^R values used in present paper are defined by those at some theoretical conditions, such as the under-aged conditions in Fig. 5 and 6 or the conditions of $f_c = 0.1$ vol.% and aged at 513 K and 463 K for the Al–Cu–Mg and Al–Mg–Si alloys, respectively, as in Figs. 7–9, all of which are constants once chosen.

The size r_i and inter-particle spacing λ_i of the three classes of second-phase particles could be related to the volume fraction f_i as $f_i = c\pi k_i(r_i/\lambda_i)^3$ ($i = c$, d and p) on the basis of the assumption of a cubic arrangement, where k_i is the aspect ratio of the particles as measured and the value of c is 2 for the non-sphere constituents and precipitates and 4/3 for the sphere dispersoids. In particular for the precipitates, r_p, λ_p and f_p are evolved with the aging treatment, as is well described by using the thermodynamics and kinetics for the precipitation process in aged aluminum alloys [25,32]. As a result, Eqs. (2) and (3) could be used for revealing the dependence of the ε_f and K_{IC} values of aluminum alloys on the aging-modulated dynamic combination of the multi-scale second-phase particles quantitatively, as shown in Figs. 5 and 6 as calculated curves. Specifically, the trade-off in the volume fraction between the constituents and the precipitates caused by the other heat treatment steps, i.e. solution and/or quenching treatments, could be considered by using Eqs. (2) and (3), respectively. For simplicity, the parameters of the dispersoids could be regarded as constant because, in the present work, the effect of the solution and/or quenching treatments on the dispersoids was

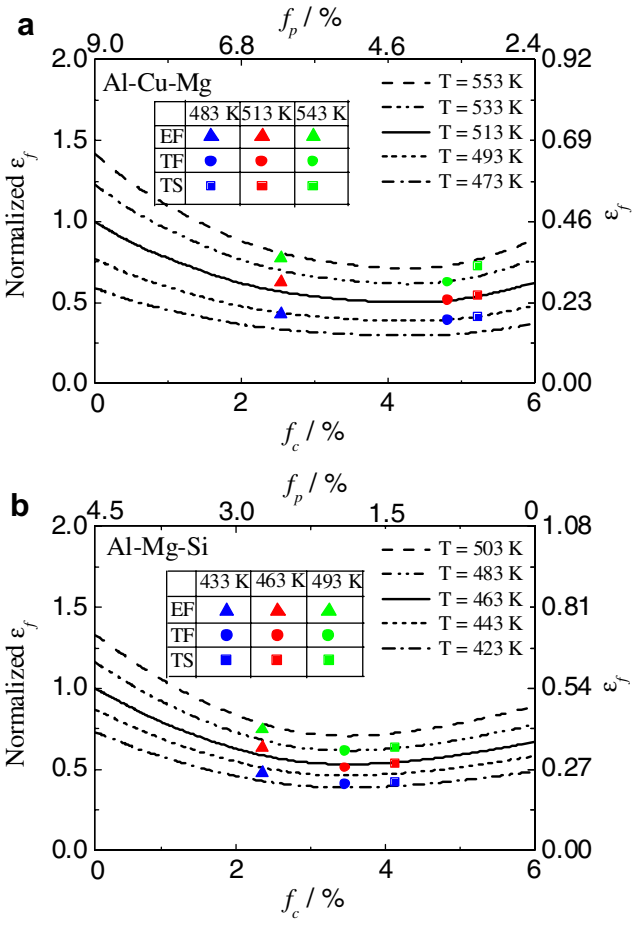

Fig. 7. Dependence of ε_f on the aging-modulated trade-off in the volume fraction between the constituents (f_c) and the precipitates (f_p) for (a) the peak-aged Al–Cu–Mg alloy and (b) the peak-aged Al–Mg–Si alloy. The dots are the experimental results and the curves are the calculated results. The reference strain to fracture ε_f^R is that of the sample with $f_c \to 0$ and aged at 513 K and 463 K for the Al–Cu–Mg alloy and the Al–Mg–Si alloy, respectively.

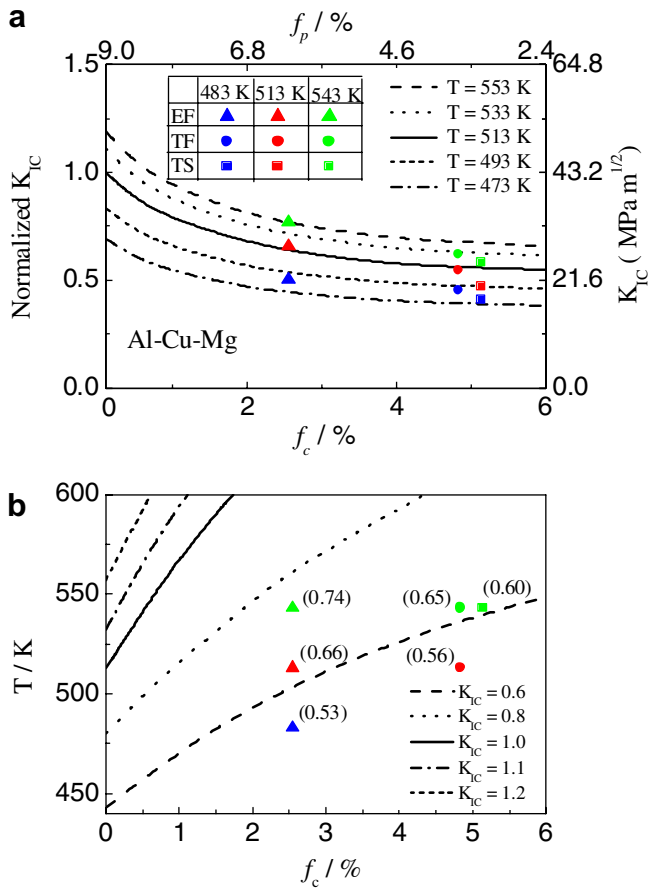

Fig. 8. (a) Dependence of the fracture toughness (K_{IC}) on the aging-modulated trade-off in the volume fraction between the constituents (f_c) and the precipitates (f_p) for the peak-aged Al–Cu–Mg alloy and (b) some contours of the normalized fracture toughness of the peak-aged Al–Cu–Mg alloy in variants of the volume fraction of the constituents (f_c) and the aging temperature (T). The dots are the experimental results and the curves are the calculated results. The reference fracture toughness K_{IC}^R is that of the sample with $f_c \to 0$ and peak aged at 513 K.

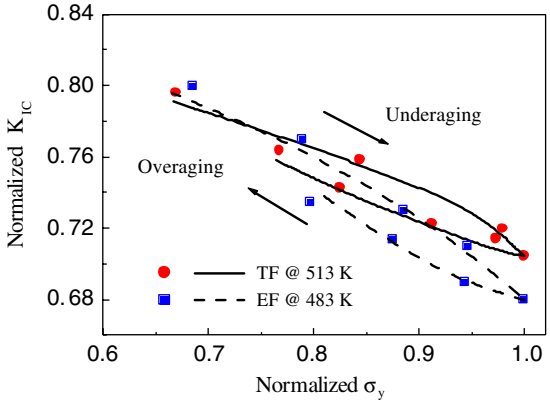

Fig. 9. Aging-modulated relationship between the normalized yield strength and the normalized fracture toughness of the TF-treated Al–Cu–Mg alloy aged at 513 K and the EF-treated Al–Cu–Mg alloy aged at 483 K. The dots are the experimental results and the curves were calculated using the multi-scale model and the strengthening model [27]. The yield strength is normalized by the maximum yield strength and the fracture toughness is normalized by K_{IC}^R as in Fig. 8.

much weaker compared with that on the constituents and the precipitates [14].

For application of the model to the experimental data, the thermodynamics and kinetics for the precipitation process were firstly obtained from the experimental results following the treatment in Ref. [25]. The dynamic evolutions of the precipitate size and volume fraction were then quantitatively presented, which could be used for calculating the evolution of the yield strength with aging temperature and aging time by using the strengthening model, as shown in the curves in Fig. 4. Moreover, the quantitative evolutions of the precipitate size and volume fraction were subsequently employed for calculating the evolution of ε_f and K_{IC} with the aging temperature and aging time by using Eqs. (2) and (3), respectively. In order to eliminate the unevaluated constants in Eqs. (2) and (3), normalization treatment was employed where an under-aged condition that aged in only 10 s was theoretically chosen as the reference. Therefore, the ε_f and K_{IC} values of the chosen condition were defined as a reference strain to the fracture (ε_f^R) and fracture toughness (K_{IC}^R), respectively and the normalized curves were calculated as shown in Figs. 5 and 6. On the other hand, the experimental results were also normalized in order to match the calculations. In fitting the normalized experimental results in the normalized calculated curves, ε_f^R was calibrated as ~0.5 and 0.6 for the Al–Cu–Mg and Al–Mg–Si alloys, respectively and K_{IC}^R was ~32.0 MPa/m$^{0.5}$ for the Al–Cu–Mg alloy. Because the aging time was chosen to be as short as 10 s, ε_f^R and K_{IC}^R were constant and not sensitive to the aging temperature. In these calculations, the parameters of the constituents and dispersoids were constant (see Ref. [12]) because only the parameters of the precipitates were variant with the aging process. With regard to the effect of the volume fraction trade-off between the constituents and precipitates on the ductile fracture, as shown in Figs. 7 and 8, the $\varepsilon_f^R(K_{IC}^R)$ value of the Al–Cu–Mg and Al–Mg–Si alloys was theoretically chosen as $\varepsilon_f(K_{IC})$ of the corresponding alloy, with $f_c \to 0$ and the alloys peak aged at 513 K and 463 K, respectively. At this point, ε_f^R was calibrated as ~0.46 and 0.54 for the Al–Cu–Mg and Al–Mg–Si alloys, respectively and K_{IC}^R was ~43.2 MPa/m$^{0.5}$ for the Al–Cu–Mg alloy. An important issue that should be noted in these calculations is that, with the change in the volume fraction of the precipitates, the precipitate size at peak-aged condition was also theoretically modified because the driving force for the precipitation and the aging time needed to achieve the peak-aged condition were both changed [32]. In Fig. 9 the yield strength was also normalized by the maximum yield strength, i.e. the one at peak-aged condition (298 MPa for the TF-treated Al–Cu–Mg alloy aged at 513 K and 407 MPa for the EF-treated Al–Cu–Mg alloy aged at 483 K), in order for the two curves to have the same scale on the abscissa.

Figs. 7a and b show the dependence of ε_f on the aging-modulated trade-off in the volume fraction between the constituents and the precipitates for the peak-aged

Al–Cu–Mg and Al–Mg–Si alloys, respectively. The dots are experimental results and the curves are the calculated results using Eq. (2). It is explicitly shown in Fig. 7 that the dependence of ε_f on the trade-off between f_c and f_p is non-monotonic and sensitive to the aging treatment or aging temperature. In other words, with the increase in f_c and the concomitant decrease in f_p, the ductility is generally found to reduce gradually down to a minimum and then rise somewhat. Moreover, the non-monotonic dependence of ε_f is shown to be more intense when aged at a higher temperature. This non-monotonic evolution of ε_f with the trade-off between f_c and f_p results from the competitive effect of the precipitates and constituents on the ductility. On the one hand, a greater volume fraction of the constituents should induce a decrease in the ductility because of the easy initiation of large voids. On the other hand, the increase in the precipitates should bring about a more intense local stress–strain concentration. As a result, the trade-off between f_c and f_p should produce competition between the detrimental influences of the precipitates and constituents, which results in a minimum ductility at a certain combination of the precipitates and constituents in both the volume fraction and size. However, when the aging temperature is changed, the size of the precipitates should be different and the combination of the precipitates and constituents will be changed. This is the aging-modulated coupling effect of the precipitates and constituents. Quantitatively, it is known that an alloy aged at lower temperatures should have precipitates of smaller size but exhibit a greater strength, which means a more intense local stress–strain concentration may be induced, which should result in a lower ductility. Therefore, compared with the ductility of the alloys aged at a reference temperature, i.e. 513 K for the Al–Cu–Mg alloy and 463 K for the Al–Mg–Si alloy, respectively, the alloys aged at lower temperatures should exhibit a smaller ductility and vice versa.

The aging-modulated coupling effect of the precipitates and constituents could be responsible for the experimental observations that the alloy containing a greater volume fraction of the detrimental constituents might have a greater ductility than the alloy containing a lesser volume fraction of the constituents. It can be seen from Fig. 7 that the EF-treated alloys aged at a lower temperature exhibited an inferior ductility to that of the TF-treated and TS-treated alloys aged at higher temperatures, although the two latter alloys contained a greater volume fraction of the constituents than the former alloys. A similar trend was found in the fracture toughness of the aluminum alloys, as shown in Fig. 8a, where the monotonic dependence of K_{IC} on the aging-modulated trade-off between f_c and f_p was always found for the Al–Cu–Mg alloys. This indicates that the influence of the constituents on the fracture toughness is overwhelming as compared to that of the precipitates.

As a further illustration, Fig. 8b shows some contours of the fracture toughness of the peak-aged Al–Cu–Mg alloys in variants of the aging temperature (T) and the volume fraction of the constituents (f_c), where the reference K_{IC}^{R} is the same as that in Fig. 8a, i.e. the theoretical fracture toughness of the Al–Cu–Mg alloy with $f_c \to 0$ but aged at 513 K. All the cooperative effects of T and f_c on a contour should produce the same fracture toughness for aged aluminum alloys. Referring to Fig. 8b, the aging temperature could be artificially chosen in order to achieve the desired fracture toughness as a function of f_c. For example, if the alloys contain more constituents than expected, a somewhat higher aging temperature could be subsequently employed for keeping the desired fracture toughness. Because f_c is closely dependent on the solution treatment and/or quenching treatment, the contours in Fig. 8b are modulated not only by the aging treatment but also by the solution treatment and/or quenching treatment. The development of contours of the fracture toughness may be helpful in providing a theory-assisted selection of the heat treatment steps for meeting the practical needs of fracture toughness for aged aluminum alloys.

The good agreement between the calculations and experimental results in Figs. 7 and 8 indicates that the present model is competent for evaluating the aging-modulated coupled influence of the constituents and precipitates on the ductility and fracture toughness of heat-treatable aluminum alloys. Of special interest to note is that the present model could be used as a good description of the effect of the aging conditions on the relationship between the yield strength and fracture toughness, as shown in Fig. 9 where the yield strength is normalized by the maximum yield strength.

4.2. Quenching-modulated coupling effect of the multi-scale second-phase particles

As mentioned earlier, the quenching treatment could make a trade-off in the volume fraction among the three classes of second-phase particles as well. When a slow quench is applied more solute atoms will precipitate to form additional second-phase particles that have no strengthening contribution and decrease the volume fraction of the strengthening precipitates. This indicates that the influence of the quench process on the ductility and fracture toughness of aluminum alloys is essentially the coupled influence of the multi-scale second-phase particles. Some limited work modeling and analyzing the quench-dependent yield strength of aluminum alloys has been performed [33–35]. Here, the quench-modulated coupling effect of the multi-scale second-phase particles on the fracture toughness will be focused and quantitatively revealed.

During the continuous cooling of aluminum alloys in the quench process, the volume fraction of newly formed constituent (f_c^q) could be given by a modified form of the Avramic-type equation as

$$f_c^q = f_c^{q,max}\{1 - \exp[-(\varphi Q)^n]\}, \quad (4)$$

where $f_c^{q,max}$ is the equilibrium volume fraction of the constituents that could precipitate from the temperature at the

start of the quench to the temperature at the finish of the quench, φ is a temperature-dependent term that dominates the phase transformation rate and the value of φ was estimated as 0.001 in the present work [32], exponent n was experimentally determined as ~1–2 [36] (in the present calculations the value of 1 was chosen for simplicity) and Q is a quench factor that is based on the C-curve and the continuous cooling quench curve as [33]

$$Q = \int_{t_0}^{t_f} \frac{dt}{C_t} \approx \sum_{i=1}^{n} \frac{dt_i}{C_{t,i}}, \tag{5}$$

where C_t is the critical time required for precipitating a constant amount of the constituents during isothermal annealing, dt is the time increment from the quench curve, t_0 is the time at the start of the quench and t_f is the time at the finish of the quench. Qualitatively, a larger quench factor Q means a prolonged quench process. Assuming that the constituents have the same composition as that of the precipitates for simplicity, the volume fraction of the precipitates will decrease due to the precipitation of some alloying atoms to form more constituents during the quench process

$$f_p = f_p^{max} - f_c^q, \tag{6}$$

where f_p^{max} is the maximum volume fraction of the precipitates that could be achieved with enough fast quench. Substituting Eq. (6) into Eq. (4) yields

$$1 - \frac{f_p^{max}}{f_c^{q,max}} + \frac{f_p}{f_c^{q,max}} = \exp[-(\varphi Q)^n]. \tag{7}$$

It has been suggested that the value of f_p^{max} was about the same as that of $f_c^{q,max}$ [33]. So Eq. (7) could be rewritten as

$$f_p/f_p^{max} = \exp[-(\varphi Q)^n]. \tag{8}$$

This equation clearly reveals that the increase in the quench factor Q or the prolongation of the quench process should make the volume fraction of the precipitates decrease and reduce the yield strength. On the contrary, the volume fraction of the constituents will increase. The total volume fraction of the constituents (f_c^t) is the sum of the initial volume before solution treatment (f_c) and the volume fraction precipitated during the quench process (f_c^q) as

$$f_c^t = f_c + f_c^q. \tag{9}$$

Substituting f_c^t and the yield strength calculated from the strengthening model [25] into Eq. (3) will give the dependence of the fracture toughness on the quench factor. For quantitative purposes, the value of f_c is chosen as that in the TF-treated conditions. Fig. 10a shows the quench-modulated dependence of K_{IC} on the aging temperature as a function of Q for the peak-aged Al–Cu–Mg alloy, where the reference fracture toughness is defined as that when $Q \approx 0$ or when the quench is enough fast. The calculated fracture toughness is found to decrease with an increasing quench factor, particularly when the quench factor exceeds 100, which is in good agreement with the experimental results. It is also quantitatively shown that the fracture toughness is less sensitive to the quench factor at a higher aging temperature. This means that an appropriate cooperation of the quenching treatment and aging treatment is necessary in order to achieve the superior fracture toughness for heat-treatable aluminum alloys.

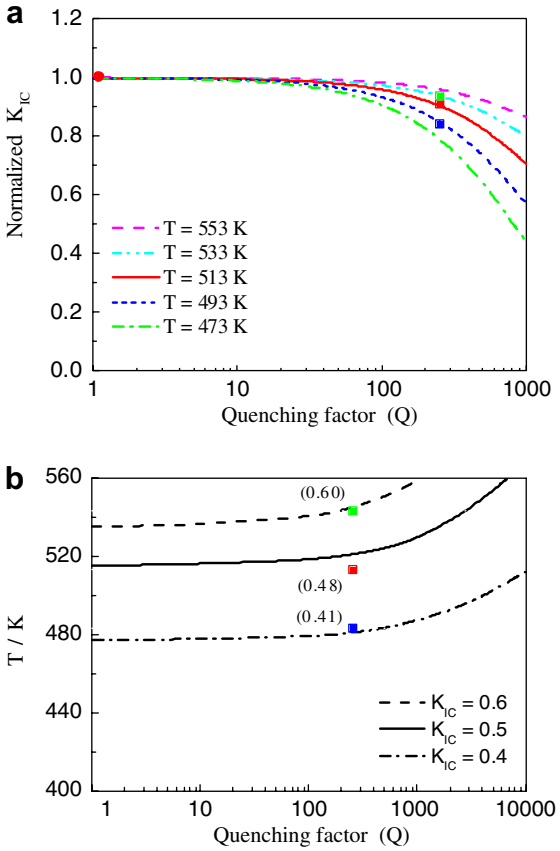

Fig. 10. (a) Dependence of the normalized K_{IC} on the aging temperature (T) as a function of the quench factor (Q) and (b) some contours of the normalized fracture toughness of the peak-aged Al–Cu–Mg alloy in variants of Q and T. The reference fracture toughness K_{IC}^R in (a) is defined as that when $Q \approx 0$ or when the quench is fast enough and K_{IC}^R in (b) is the same as in Fig. 8. The green, red and blue dots are the experimental results of the TS-treated sample peak aged at 543 K, 513 K and 483 K, respectively and the curves are the calculated results. (For interpretation of the references to color in this figure legend, the reader is referred to the web version of this article.)

Fig. 10b shows some typical contours of fracture toughness of the peak-aged Al–Cu–Mg alloys in variants of the aging temperature and quench factor Q, where the reference K_{IC}^R is the same as that in Fig. 8 and is smaller than the reference fracture toughness in Fig. 10a. The agreement between the experimental and calculated results as shown from Fig. 10b indicates that it is possible to select an aging treatment artificially to match the foregoing quenching treatment in order to achieve a cooperation effect for obtaining the desired fracture toughness for heat-treatable aluminum alloys, which may be helpful in favoring practical production in industry.

5. Conclusions

1. The alloys containing less detrimental constituents but aged at a lower temperature were experimentally found to exhibit a ductility and fracture toughness inferior to those of the alloys containing more detrimental constituents but aged at a somewhat higher temperature, which is applicable for two typical kinds of heat-treatable aluminum alloys. A multi-scale model is presented to explain this phenomenon reasonably by revealing the aging-modulated coupling influence of the multi-scale second-phase particles. Based on this model, the quench rate-dependent fracture toughness is quantitatively evaluated for heat-treatable aluminum alloys.
2. The contours of the fracture toughness of heat-treatable aluminum alloys with respect to the volume fraction of the constituents and the aging temperature and to the quench factor and the aging temperature have been developed, respectively, which could be helpful in optimizing the coupling effect of the multi-scale second-phase particles by artificially selecting the heat treatment steps in order to achieve the desired fracture toughness.
3. The experimental and calculated results revealed that an appropriate cooperation of the solution, quenching and aging treatments or an appropriate combination of the multi-scale second-phase particles is necessary and sufficient for achieving an excellent fracture toughness for heat-treatable aluminum alloys. Any single improvement in the solution, quenching or aging treatments is not enough to ensure a superior fracture toughness.

Acknowledgments

The National Basic Research Program of China supported this research (Grant nos. 2004CB619303 and 2005CB623700). The authors also express their special thanks for the support of the National Natural Science Foundation of China and the National Outstanding Young Investigator Grant of China. The Program for Changjiang Scholars and Innovative Research Team in University and the 111 program of China (under Grant No. B06025) also supported this work.

References

[1] Hahn GT, Rosenfield AR. Metall Trans A 1975;6:653.
[2] Thompson DS. Metall Trans A 1975;6:671.
[3] Garrett GG, Knott JF. Metall Trans A 1978;9:1187.
[4] Broek D. Eng Fract Mech 1973;5:55.
[5] Van Stone RH, Psioda JA. Metall Trans A 1975;6:668.
[6] Staley JT. Aluminum 1979;55:277.
[7] Hornbogen E, Starke Jr EA. Acta Metall 1993;41:1.
[8] Cox TB, Low Jr JR. Metall Trans 1974;5:459.
[9] Walsh JA, Jata KV, Starke EA. Acta Metall 1989;37:2861.
[10] Prince KC, Martin JW. Acta Metall 1979;27:1401.
[11] Liu G, Zhang GJ, Ding XD, Sun J, Chen KH. Metall Mater Trans A 2004;35:1725.
[12] Liu G, Sun J, Nan CW, Chen KH. Acta Metall 2005;53:3459.
[13] Clouet E, Barbu A, Lae L, Martin G. Acta Metall 2005;53:2313.
[14] Robson JD. Acta Metall 2004;52:1409.
[15] Robson JD, Prangnell PB. Acta Metall 2001;49:599.
[16] Bratland DH, Grong Ø, Shercliff H, Myhr OR, TjØtta S. Acta Metall 1997;45:1.
[17] Myhr OR, Grong Ø. Acta Mater 2000;48:1605.
[18] Grong Ø, Shercliff HR. Prog Mater Sci 2002;47:163.
[19] Starink MJ, Wang SC. Acta Mater 2003;51:5131.
[20] Nicolas M, Deschamps A. Acta Mater 2003;51:6077.
[21] Esmaeili S, Lloyd DJ, Poole WJ. Acta Mater 2003;51:3467.
[22] Shercliff HR, Ashby MF. Acta Mater 1990;38:1789.
[23] Deschamps A, Brechet Y. Acta Mater 1999;47:293.
[24] Starink MJ, Wang P, Sinclair I, Gregson PJ. Acta Mater 1999;47:3855.
[25] Liu G, Zhang GJ, Ding XD, Sun J, Chen KH. Mater Sci Eng A 2003;344:113.
[26] Zhu AW, Starke Jr EA. Acta Mater 1999;47:3263.
[27] Haynes MJ, Gangloff RP. J Test Eval 1997;25:82.
[28] DeHoff RT, Rhines FN. Quantitative microscopy. New York (NY): McGraw-Hill; 1968.
[29] Crompton JMG, Waghorne RM, Brook Jr CB. J Appl Phys 1966;16:277.
[30] Gilmore DL, Starke Jr EA. Metall Mater Trans A 1997;28:1399.
[31] Edington JW. Practical electron microscopy in materials science. London: Van Nostrand Reinhold Company; 1976. p. 207.
[32] Liu G. PhD Thesis, Xi'an Jiaotong University, Xi'an; 2002.
[33] Staley JT. Mater Sci Tech 1987;3:923.
[34] Staley JT, Doherty RD, Jaworski AP. Metall Trans A 1993;24:43.
[35] Rometsch PA, Starink MJ, Gregson PJ. Mater Sci Eng A 2003;339:255.
[36] Serve I, Turnbull D. Acta Mater 1966;14:167.